Bipolar nanochannels: The effects of an electroosmotic instability. Part I: Steady-state response

Ramadan Abu-Rjal and Yoav Green[†]

Department of Mechanical Engineering, Ben-Gurion University of the Negev, Beer-Sheva 8410501, Israel

† yoavgreen@bgu.ac.il

Supplementary Materials

Contents

1. Numerical scheme

While Part I focuses on steady-state and Part II focuses on the time transient response, the numerical simulations are the same for both parts. To that end, we will discuss all issues related to numerical simulations in the Supplementary Material of Part I. We acknowledge that in this discussion, we will show two time-transient movies. The presentation of these movies here is not for scientific sake but rather for numeric sake.

1.1 *Methods.*

The main text governing equations, Eqs. (2)-(5), with boundary conditions, Eqs. (10)-(14) were solved by the commercial finite element-based software COMSOL Multiphysics. Specifically, the Transport of Diluted Species, Electrostatic, and Creeping Flow modules were simultaneously solved with a time-dependent solver.

To compute our time-dependent solution, we used a direct solution method, namely the multifrontal massively parallel solver (MUMPS), based on Gaussian factorization. The implicit Backward Differentiation Formula (BDF) solver was employed as the time-stepping method. The solver automatically determines the time steps to satisfy the specified relative tolerance (its value was set to 10^{-3}). To better capture the system response, we used very small output time (the times at which the solution is stored for postprocessing and evaluation) steps for earlier times. Depending on the applied voltage, we increased it gradually for later times. Namely, as the applied voltage increases, the output time stepping decreases for later times.

1.2 *Initial conditions.*

The initial conditions used in all simulations are the equilibrium states that account for the electrical double layers (EDLs) at the interfaces. To find these equilibrium states, we considered a simplified situation whereby the initial conditions were $c_{\pm,1,4} = 1$, $c_{+,2} = c_{-,2}^{-1} = N_2$, and $c_{+,3}^{-1} = c_{-,3} = -N_3$ (subscript numbers denote regions) with an applied potential difference $V = 0$. We let the system relax to its actual equilibrium state. The resultant solutions that account for the EDLs are then used as our initial conditions.

1.3 *Simulation parameters*

The simulation parameters used in Part I and Part II are provided in **Table S1** and **Table S2**. **Table S1** lists the dimensionless parameters that were held constant across all simulations. **Table S2** provides the ranges of the dimensionless parameters N_3, $L_{3,4}$, and V as they are varied in each section. **Table S3** lists all the characteristics parameters needed for the non-dimensional parameters.

Table S1: *Simulation dimensionless parameters used for all simulations in Part I and Part II.*

	Value
Region lengths, $L_{1,2}$	1
Region width, W	2
Fixed charge density, N_2	25
Debye length, ε	10^{-3}
Péclet number, Pe	0.5

Table S2: *Region 3 fixed charge density, N_3, and length, L_3, Region 4 length, L_4, and voltage, V, used in the simulations of each section.*

	N_3	L_3	L_4	V
Part I – Sec. 4	[−25,0]	1	1	[−80,80]
Part I – Sec. 4; Part II – Sec. 3.	0	0	1 or 2	[−80,80]
Part I – Sec. 4; Part II – Sec. 4.	−25	1	1	[−100,100]
Part I – Sec. 4; Part II – Sec. 5.	−10	1	1	[−80,80]

Table S3: *The characteristics parameters of a binary electrolyte solution and a system needed for calculating dimensionless parameters.*

Parameter	Value
Diffusion coefficient, $\tilde{D}$	$10^{-9}\,[\text{m}^2/\text{s}]$
Relative permittivity, ε_r	78.4
Dynamic viscosity, $\tilde{\mu}$	$9\times10^{-4}\,[\text{Pa}\times\text{s}]$
Absolute temperature, $\tilde{T}$	298[K]
Bulk concentration, $\tilde{c}_0$	$0.01\,[\text{mol}/\text{m}^3]$
Region length, $\tilde{L}$	$100\,[\mu\text{m}]$

We note here that we chose the diffusion coefficient to be half of the typical value of KCl (**Table S3**). This was done so that our simulation parameters would be consistent with the simulation parameters of Rubinstein and Zaltzman (Rubinstein & Zaltzman, 2000; Zaltzman & Rubinstein, 2007). Taking the correct value would reduce Pe by a factor. Thereafter, all the observed phenomena would appear qualitatively unchanged but with some slight quantitative changes.
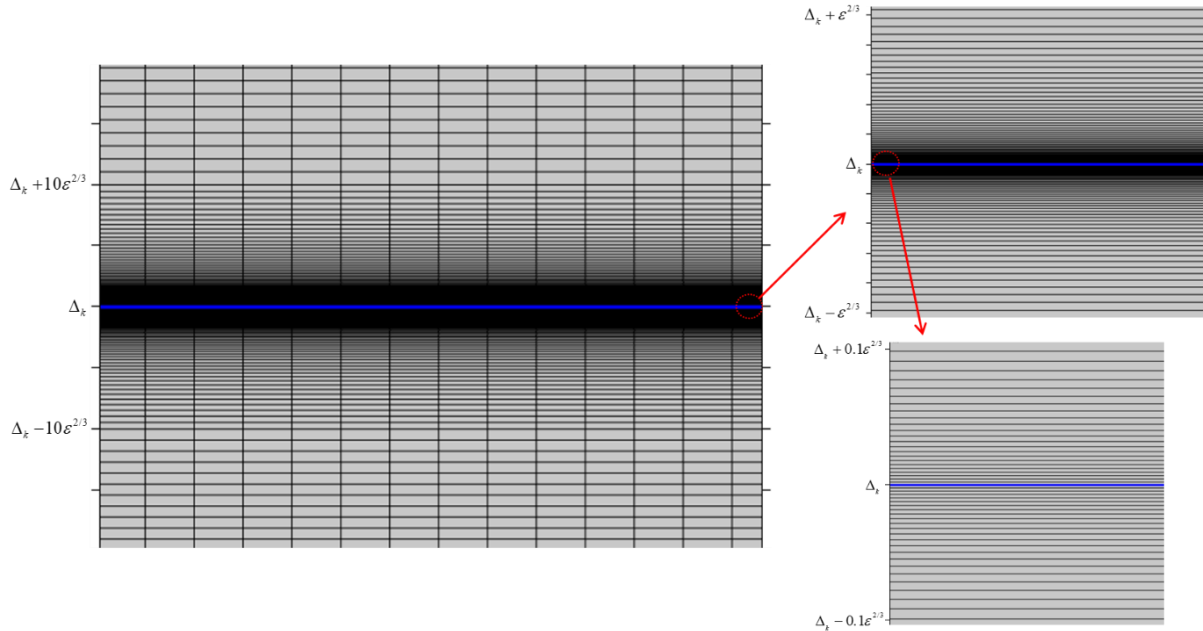
1.4   Meshing
To ensure that our final results are mesh-independent, while the strong variations at the interfaces, which are mesh-dependent, do not change the overall response, we varied the mesh for several scenarios. We show that the overall response does not change the response.

1.4.1   Meshing in 2D
To resolve the strong variations in the EDLs near the three interfaces located at $y = \Delta_{k=1,2,3}$, a non-uniform mesh was used in the y-direction normal to the interfaces with high refinement near the interfaces, while a uniform mesh was used in the tangential x-direction (Demekhin, Nikitin, & Shelistov, 2013; Karatay, Druzgalski, & Mani, 2015). In the y-direction, we used a refined mesh near each interface $\Delta_{k=1,2,3}$ within the domains $[\Delta_{k=1,2,3} - 10\varepsilon^{2/3}, \Delta_{k=1,2,3} + 10\varepsilon^{2/3}]$ (see **Figure S1**). In these domains, 101 mesh points were used on each side of $\Delta_{k=1,2,3}$ to create meshes that were smallest at $y = \Delta_{k=1,2,3}$ and largest at $y = \Delta_{k=1,2,3} \pm 10\varepsilon^{2/3}$. To that end, we used the geometric series distribution option with a ratio of 250 between the small grid size 2.178×10^{-5} (on both sides of $\Delta_{k=1,2,3}$ and near the interface itself) and largest grid size, 5.445×10^{-3} (far from the interface). In

our simulations, the EDL value was $\varepsilon = 10^{-3}$, such that we were able to capture most of the changes very smoothly. Outside of these highly refined domains, 100 uniform mesh points were used in each region, with grid sizes of approximately 9×10^{-3}. As we will discuss shortly, while our number of elements for 2D simulations was 100 in the refined domain, we also considered 10^3 and 10^4 for 1D simulations, where it will be observed that outside of the EDLs, there are no changes, while inside, there are small changes. Our choice of 100 elements was to ensure that the simulations were tractable.


Figure S1. *The mesh used in the numerical simulations near one of the interfaces. The mesh is structured to capture the sharp changes within the EDL.*

1.4.2   *The differences between meshing in a 2D system vs. a 1D system*

This work calculates the various fields and their derivatives (which yield the fluxes). When calculating the fluxes $\overline{j}$ and $\overline{i}$, we noticed that there are large, almost discontinuous, jumps near the interfaces located at $y = \Delta_1, \Delta_2, \Delta_3$. These jumps occur regardless of whether we are considering a 1D system without EOF (**Figure S2**) or a 2D system either without EOF (**Figure S3**) or with EOF (not shown here). In the following, we will demonstrate that these spikes are a numerical artifact, and then we will discuss how we filter these spikes from our data to create "smoother" videos for the fluxes.

Our previous work (Abu-Rjal & Green, 2021) focused on 1D convectionless systems. Since the system was 1D, we could mesh the interfaces in a highly resolved manner without considerable computation costs, such that the discontinuities were relatively small. However, our current setup differs in that we account for convection, which requires considering a 2D system. As a result, the computational costs increase substantially. **Figure S2** demonstrates that in a pure 1D system, the magnitude of the spike decreases as the number of elements increases. Further, it can be observed that at a distance of ε from the interfaces, all the electrical currents are the same regardless of the spike, indicating that outside the $O(\varepsilon)$ boundary layers, the results are independent of numerics. Further, since the ESC is of order $O(\varepsilon^{2/3})$, all of the meshes capture the structure of the ESC quite well.
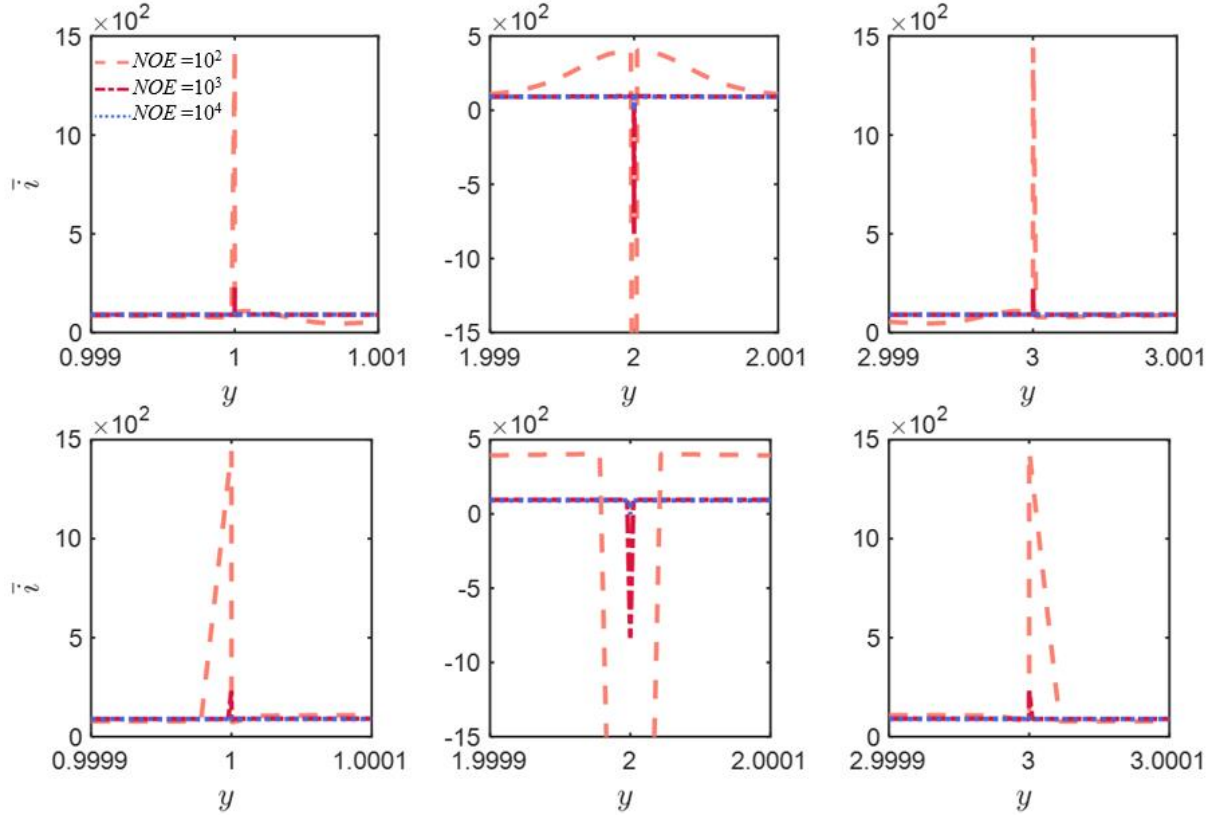
Figure S2. *The electric current,* $\bar{i}$*, near the interfaces* $y = \Delta_1, \Delta_2, \Delta_3$ *in 1D simulations for different meshes, with varying number of elements (NOE) in the domains* $[\Delta_{k=1,2,3} - 10\varepsilon^{2/3}, \Delta_{k=1,2,3} + 10\varepsilon^{2/3}]$*. In the top row, we plot* $\bar{i}$ *in the domain* $[\Delta_{k=1,2,3} - \varepsilon, \Delta_{k=1,2,3} + \varepsilon]$ *and the bottom row, we plot* $\bar{i}$ *in the smaller domain* $[\Delta_{k=1,2,3} - \frac{1}{10}\varepsilon, \Delta_{k=1,2,3} + \frac{1}{10}\varepsilon]$*.*
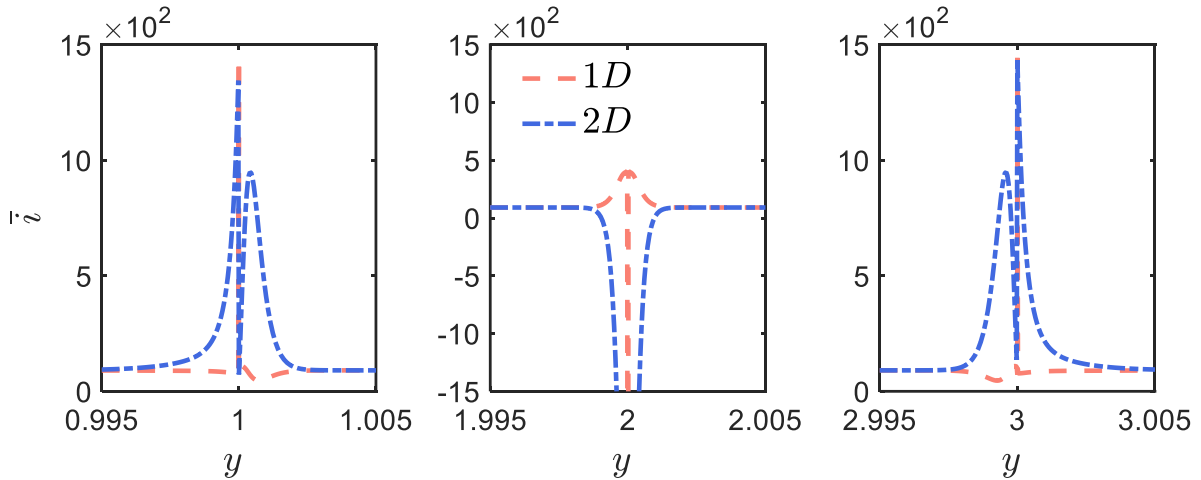
Figure S3. *The electric current,* $\bar{i}$*, near the interfaces* $y = \Delta_1, \Delta_2, \Delta_3$ *in 1D and 2D convectionless simulations for number of elements* $\text{NOE} = 100$ *in the domains* $[\Delta_{k=1,2,3} - 10\varepsilon^{2/3}, \Delta_{k=1,2,3} + 10\varepsilon^{2/3}]$*.*

A similar behavior can be observed in **Figure S3**, where we compare the numerical simulations of the electrical current for a 1D and 2D convectionless system. As can be expected, within the boundary layer, the response differs. This can be expected as meshing effects from the transverse direction become non-negligible. In contrast, outside of the $O(\varepsilon)$ boundary layers, the electrical current is independent of the meshing. Once more, this indicates that our chosen mesh is suitable for our simulations.

Finally, in our past works (Green, Edri, & Yossifon, 2015; Abu-Rjal & Green, 2021), we have shown that in a 1D system, the x-average electrical current density, i, is a constant (i.e., it is independent of y) throughout the system. Indeed, we see in **Figure S2** and **Figure S3** that this is the case everywhere except near the three interfaces $y = \Delta_1, \Delta_2, \Delta_3$. We use this understanding to improve the presentation of our fluxes movies (**Movies 3**, **6,** and **9**) so that all the fluxes can be observed within reasonable limits. We have used a simple "filter", described in the paragraph below, that removes the spiked regions. Beforehand, we note that, from visual inspections, the fields themselves ($c_{\pm}, \rho, u, v$) are smooth, and discontinuities cannot be observed. The discontinuities (the 'spikes') are observed <u>only</u> in the fluxes.

Since the electrical current is spatially independent, except near the interfaces, we require that the ratio

$$\frac{\left| \bar{i}(y_n, t) - \bar{i}(0, t) \right|}{\left| \bar{i}(y_n, t) \right|} < err \; ,$$

is smaller than a numerical error. Here, n is the grid point number in the y-direction and err is the relative error, which we choose to be $err = 10^{-4}$. All points that satisfy this constraint are marked with a '1', and those that do not are marked with a '0', creating a vector that varies at each time step. At each step, we apply the vector to the remaining fluxes ($j_{\pm}, j$). Finally, we note that, as can be observed in **Figure S2** and **Figure S3**, the spikes are primarily located near the interfaces within the ESC, whose length is of order $O(\varepsilon^{2/3})$. We now demonstrate how the time-dependent fluxes of those shown in **Figure S2** vary. In particular, **Movie S1** shows the time-dependent behavior of the electrical current for a varying number of elements, while **Movie S2** shows the behavior of the remaining fluxes for the scenario of NOE $=1000$. The movies of fluxes in Part II will implement this smoothing filter.

2. Supplement to the main text

2.1 *Reversal of depletion and enrichment regions*

In the main text, we stated that in unipolar systems, when $V > 0$ is switched to $V < 0$, the depleted and enriched regions switch between Regions 1 and 4. Namely, for positive voltage, Region 1 is depleted and Region 4 is enriched, whereas for negative voltage, a reversal occurs. **Figure S4** demonstrates this in an asymmetric unipolar system ($2L_1 = L_4$). For the sake of simplicity, we have considered the convectionless ($Pe = 0$) steady-state response while we have varied V. The simulation values here match those given in **Table S2**.
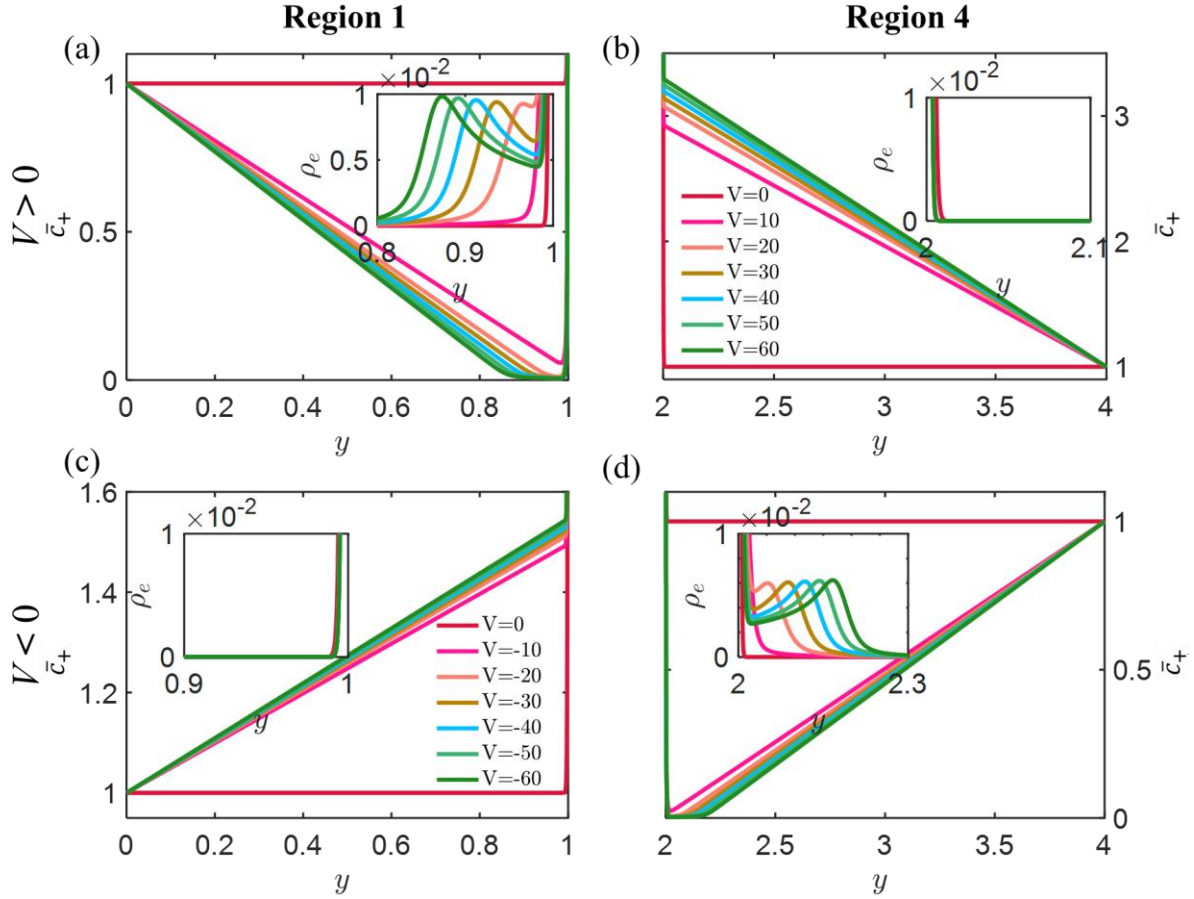
Figure S4. *Ion concentrations, c_+, of the quiescent steady state for several positive (a and b) negative voltages (c and d) in Region 1 and Region 4 of an asymmetric unipolar system ($2L_1 = L_4$). The insets show the corresponding space charge density, $\rho_e = c_+ - c_-$. Simulation parameters are given in **Table S1** and **Table S2**.*

2.2   *Vortex array stability in non-ideal bipolar systems*

Figure S5 illustrates the mixing process in a non-ideal bipolar system ($N = -10$) for several applied voltages. These snapshots of the concentration field and velocity streamlines in Region 1 are given at the same time step of $t = 10$ (which coincides with the end of our simulations). Note that as the voltage increases, the mixing becomes stronger (such that the orange region is "further compressed"). Around $V = 50$, we observe the breakdown of the periodic array and the appearance of a "chaotic motion" (Druzgalski, Andersen, & Mani, 2013). As the voltage is increased, this additional motion is responsible for increasing the current.
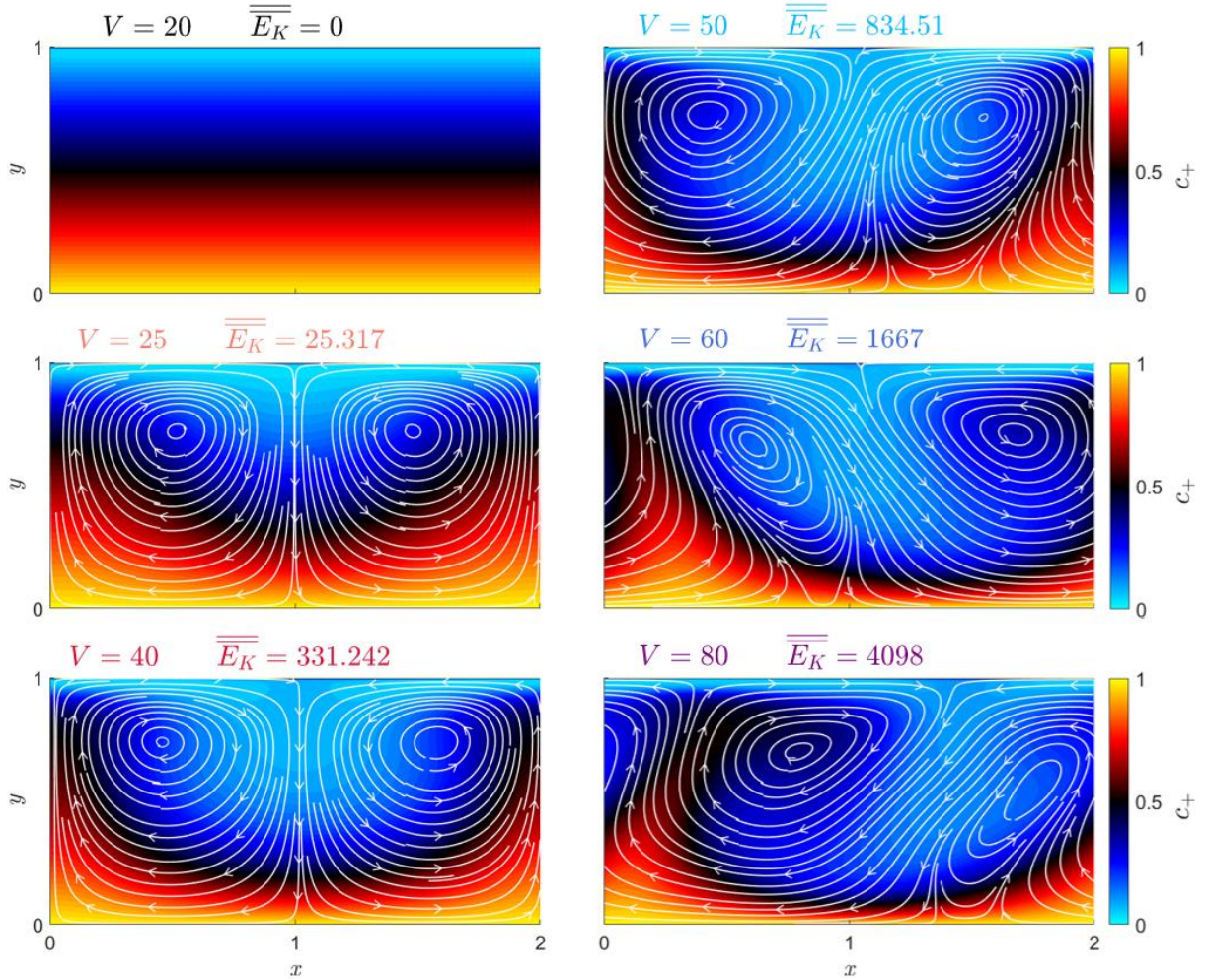
Figure S5: *The positive concentration (2D color plot), c_+, and velocity streamlines (white lines) in Regions 1 of a non-ideal bipolar system ($N_3 = -10$) for several applied voltages at the same time step of $t = 10$. The surface average of the kinetic energy, $\overline{\overline{E_k}}$, is given for each snapshot.*

2.3 *Critical voltage, V_{cr}, vs $|N_3|$*

Figure S6(a) plots the dependence of the critical voltage of the onset of EOI on $|N_3|$. It can be observed that as $|N_3|$ increases, so does the critical voltage until it plateaus at the critical voltage of the ideal scenario. This can be attributed to the variation of the overall permselectivity of the system with N_3 (Abu-Rjal et al., 2014; Abu-Rjal & Green, 2021). **Figure S6**(b) shows the behavior of the steady-state space charge density, ρ_e, for two given voltages [(b1) $V = 20$ and (b2) $V = 40$, both of which are above the critical voltage for the unipolar system] for varying values of N_3. For $V = 20$, only the unipolar system ($N_3 = 0$, given by the pink line) has an ESC – which leads to EOI. While for $V = 40$, all values with $|N_3| < 20$ have an ESC and thus can support EOI. In both voltages, it can be observed that the unipolar system has the most pronounced ESC

(maximal value and extent/length). As $|N_3|$ increases, the effects of the ESC become less pronounced, to the point that the ideal bipolar system ($N_3 = -N_2$, given by the purple line) is still in its quasi-equilibrium state.
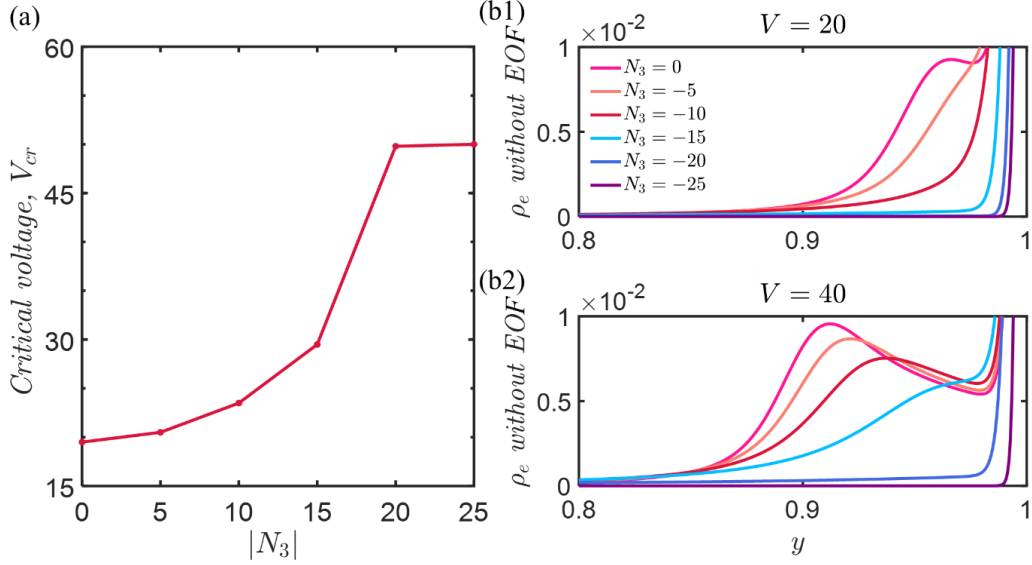
Figure S6: *(a) The dependence of the critical voltage of the EOI onset, V_{cr}, on $|N_3|$. (b) The space charge density ρ_e without EOI near the interface in Region 1 for different N_3, and for (b1) $V = 20$ and (b2) $V = 40$.*

2.4   *Kinetic energy scaling with $V - V_{cr}$*

Figure S7 presents intriguing empirical correlations between $\left\langle \overline{\overline{E_k}} \right\rangle$ in Region 1 and $(V - V_{cr})^2$ for several values of N_3. In all scenarios, it can be observed that there is the following parabolic dependence $\left\langle \overline{\overline{E_k}} \right\rangle = \alpha [V - V_{cr}]^2 + \beta$, where α and β are fitting parameters. It is evident that as $|N_3|$ increases, both α and β decrease, eventually reaching $\alpha(\eta = 1) = \beta(\eta = 1) = 0$ for the ideal bipolar scenario (not shown here since $\left\langle \overline{\overline{E_k}}(\eta = 1) \right\rangle \triangleq 0$). It is obvious that α and β vary with N_3 and N_2 (i.e., η), and possibly other variables, including the geometry. However, thus far, our attempts to curve fit α and β have been unsuccessful – the reason is that the underlying rationale for their dependence on N_2 and N_3 is not understood, and therefore, our attempts have used rather simplistic guesses. Future work is needed to clarify the dependence of α and β on all system parameters.
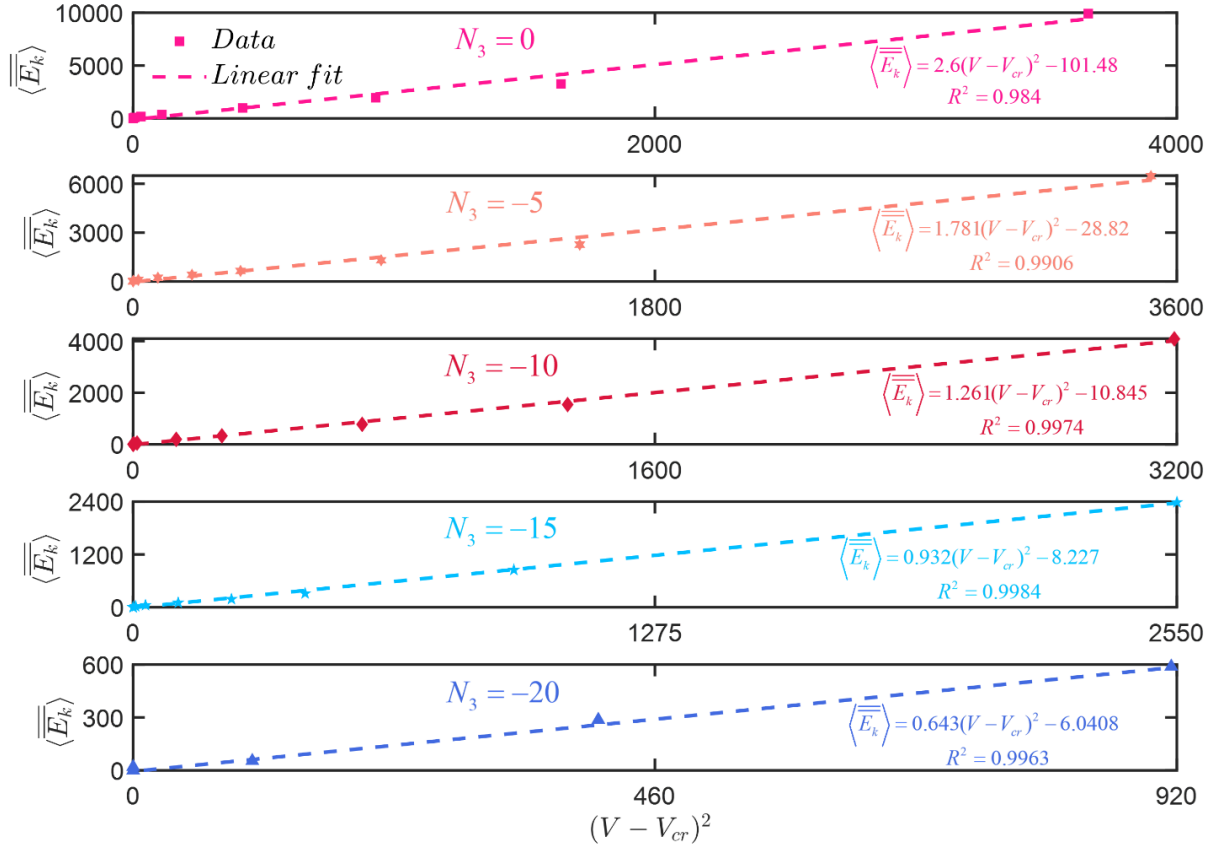
Figure S7: *The steady-state surface average of the kinetic energy,* $\left\langle \overline{\overline{E_k}} \right\rangle$, *in Region 1 vs* $(V - V_{cr})^2$ *for several values of* N_3. *The curve-fitted values for* α *and* β *are given, as well as the coefficient of determination,* R^2.

For the subplots (with $\left\langle \overline{\overline{E_k}} \right\rangle$ on the vertical axis and $(V - V_{cr})^2$ on the horizontal axis):

- $N_3 = 0$: $\left\langle \overline{\overline{E_k}} \right\rangle = 2.6(V - V_{cr})^2 - 101.48$, $R^2 = 0.984$
- $N_3 = -5$: $\left\langle \overline{\overline{E_k}} \right\rangle = 1.781(V - V_{cr})^2 - 28.82$, $R^2 = 0.9906$
- $N_3 = -10$: $\left\langle \overline{\overline{E_k}} \right\rangle = 1.261(V - V_{cr})^2 - 10.845$, $R^2 = 0.9974$
- $N_3 = -15$: $\left\langle \overline{\overline{E_k}} \right\rangle = 0.932(V - V_{cr})^2 - 8.227$, $R^2 = 0.9984$
- $N_3 = -20$: $\left\langle \overline{\overline{E_k}} \right\rangle = 0.643(V - V_{cr})^2 - 6.0408$, $R^2 = 0.9963$

Legend: ■ Data, -- Linear fit

3. Movie Descriptions

Movie name	Section #	Description
Movie S1	Supplementary Material, Sec. 1.4	The time-dependent behavior of the electrical current near the interfaces $y = \Delta_1, \Delta_2, \Delta_3$ in 1D simulations for varying number of elements (NOE).
Movie S2	Supplementary Material, Sec. 1.4	The time-dependent behavior of $j_\pm, j$ near the interfaces $y = \Delta_1, \Delta_2, \Delta_3$ in 1D simulations for the scenario of NOE $= 10^4$.

References

Abu-Rjal, R., Chinaryan, V., Bazant, M. Z., Rubinstein, I., & Zaltzman, B. (2014). Effect of concentration polarization on permselectivity. *Physical Review E*, *89*(1), 012302. https://doi.org/10.1103/PhysRevE.89.012302

Abu-Rjal, R., & Green, Y. (2021). Bipolar Nanochannels: A Systematic Approach to Asymmetric Problems. *ACS Applied Materials & Interfaces*, *13*(23), 27622–27634. https://doi.org/10.1021/acsami.1c05643

Demekhin, E. A., Nikitin, N. V., & Shelistov, V. S. (2013). Direct numerical simulation of electrokinetic instability and transition to chaotic motion. *Physics of Fluids*, *25*(12), 122001. https://doi.org/10.1063/1.4843095

Druzgalski, C. L., Andersen, M. B., & Mani, A. (2013). Direct numerical simulation of electroconvective instability and hydrodynamic chaos near an ion-selective surface. *Physics of Fluids*, *25*(11), 110804. https://doi.org/10.1063/1.4818995

Green, Y., Edri, Y., & Yossifon, G. (2015). Asymmetry-induced electric current rectification in permselective systems. *Physical Review E*, *92*(3), 033018. https://doi.org/10.1103/PhysRevE.92.033018

Karatay, E., Druzgalski, C. L., & Mani, A. (2015). Simulation of chaotic electrokinetic transport: Performance of commercial software versus custom-built direct numerical simulation codes. *Journal of Colloid and Interface Science*, *446*, 67–76. https://doi.org/10.1016/j.jcis.2014.12.081

Rubinstein, I., & Zaltzman, B. (2000). Electro-osmotically induced convection at a permselective membrane. *Physical Review E*, *62*(2), 2238–2251. https://doi.org/10.1103/PhysRevE.62.2238

Zaltzman, B., & Rubinstein, I. (2007). Electro-osmotic slip and electroconvective instability. *Journal of Fluid Mechanics*, *579*, 173–226. https://doi.org/10.1017/S0022112007004880